AIAA Aviation Forum and ASCEND co-located Conference Proceedings
29 July - 2 August 2024, Las Vegas, Nevada
AIAA AVIATION FORUM AND ASCEND 2024

10.2514/6.2024-3870

Towards an immersed-boundary resolvent analysis framework for wall-bounded flows with various surface configurations

Zoey Flynn *
University of Illinois at Urbana-Champaign

H. Jane Bae †
California Institute of Technology

Andres J. Goza ‡
University of Illinois at Urbana-Champaign

New flow control paradigms for wall-bounded flows are leveraging increasingly sophisticated actuation strategies targeted near the wall surface including riblets, anisotropic porous and textured surfaces, and passively adaptive metamaterials. This new direction brings a growing need for predictive computational tools that can accurately and efficiently account for these complex surface effects, potentially involving fully coupled fluid-structure interactions (FSI). The resolvent analysis framework is a natural choice for these aims, as it provides a fast computational model rooted in an analysis of the true linearized operator for the wall-bounded flows of interest. Yet, while there are a number of resolvent-based strategies designed to incorporate surface effects, most are formulated for a specific configuration and cannot be readily extended to different setups. We present developments towards a more general formalism rooted in an immersed boundary (IB) treatment of the surface that we call IB resolvent. The proposed method inherits the benefits of versatile flow-surface treatment that high-fidelity IB methods have enjoyed for decades, formally incorporated into a spanwise-streamwise-temporal homogeneous resolvent framework that has become a workhorse for wall-bounded flow analysis and control design. We present the mathematical formulation for the case of turbulent channel flow with a static sinusoidal wall boundary condition and examine its performance. We also demonstrate that when the wall is equivalent to a flat surface, the IB resolvent results match those of the conventional resolvent analysis. While the results are focused on this canonical setting, the derivation is constructed to facilitate straightforward extensions to more complex configurations.

I. Nomenclature

$\boldsymbol{\chi}$	=	surface point coordinate
$\boldsymbol{\chi}_0$	=	undeformed surface point coordinate
$\mathbf{R}, \mathbf{E}$	=	quadrature matrices
Δy	=	wall-normal grid spacing
δ	=	delta function
$\boldsymbol{f} = (f_x, f_y, f_z)$	=	nonlinear forcing
$\mathcal{F}$, $\hat{(\cdot)}$	=	Fourier transform
g	=	geometry function of the spatially varying surface
Γ	=	immersed boundary surface
h	=	channel half height
I	=	identity matrix
$\boldsymbol{k} = (k_x, k_z, \omega)$	=	streamwise and spanwise wavenumbers and temporal frequency

*Graduate research assistant, Aerospace Engineering, 104 S Wright St, Urbana, IL 61801
†Assistant Professor, Graduate Aerospace Laboratories, 1200 East California Boulevard Pasadena, California 91125, AIAA Senior Member
‡Assistant Professor, Aerospace Engineering, 104 S Wright St, Urbana, IL 61801, AIAA Member

L	=	linearized Navier-Stokes equations
n_y	=	number of wall-normal grid points
n_{k_x}	=	number of resolved streamwise wavenumbers
ν	=	kinematic viscosity
p	=	fluid pressure
Φ	=	principal resolvent forcing mode
Ψ	=	principal resolvent response mode
q	=	state vector
Re	=	Reynolds number
Re_τ	=	friction Reynolds number
$\boldsymbol{s}$	=	surface force
σ	=	resolvent singular values
t	=	time
$\bar{\boldsymbol{u}}$	=	averaged fluid velocity field in the streamwise and spanwise directions and time
$\boldsymbol{u} = (u_x, u_y, u_z)$	=	fluid velocity field in the streamwise, wall-normal, and spanwise directions
$\boldsymbol{u}_B$	=	wall fluid velocity
u_τ	=	friction velocity
$\boldsymbol{x} = (x, y, z)$	=	flow point coordinate in the streamwise, wall-normal, and spanwise directions

II. Introduction

There is a growing pursuit of flow control strategies for wall-bounded flows that leverage complex surface actuation paradigms. These control methodologies often lead to complex boundary conditions that can be difficult to model. Moreover, the surface designs or actuation strategies can vary widely. These surface effects include simple mechanical structures like vortex generators and riblets that initiate mixing in the flow [1, 2], as well as jets with complex blowing/suction patterns [3, 4]. In recent years there has also been a growing focus on problems involving compliant, heterogeneous surfaces (and sub-surfaces), often comprised of metamaterials with the potential to have curated interactions with the flow. One example is phononic materials which contain alternating layers of material to dampen specific frequencies in the surrounding flow [5, 6]. These new materials introduce additional modeling challenges because of the fully coupled FSI that they induce in the surrounding flow.

This surface-based control pursuit has driven a need for a fast, predictive framework that enables the effective design and use of these modern surfaces and actuation strategies. Resolvent analysis is a natural foundation to use for this framework, since it provides fast models rooted in an analysis of the forced response of the true linear operator in a turbulent flow, producing clearly delineated optimal flow features as well as the optimal forcing and response of the turbulent flow [7]. The operator-based nature of the method also removes the need for large data sets. In its original form, resolvent analysis is limited to problems with stationary, smooth walls, and a number of researchers have developed extensions to more complex boundary conditions. Chavarin and Luhar [8] introduced a modified resolvent analysis for riblets through the inclusion of a volume penalization term. Luhar et al. [9] applied resolvent analysis to compliant surface problems, using linearized boundary conditions for the motion of the wall. Jafari et al. [10] developed a resolvent framework for frequency-tuned walls via a surface impedance operator that can account for various surface geometries. Another work by Luhar et al. [11] extended resolvent analysis to include functionality for opposition control, which models blowing and suction forces at the surface to suppress certain wall structures. These methods have demonstrated a utility for resolvent analysis to assess these complex surface effects, but also involve formulations that require different alterations to the boundary conditions and/or fluid-structure coupling for each problem setup considered.

This observation motivates us to develop a versatile formulation that allows different surface effects, potentially including fully coupled FSI, to be freely swapped in and out as needed. Our formalism incorporates an IB framework into resolvent analysis, whereby a delta function is used to communicate between quantities belonging to the flow domain and those belonging to the surface [12]. The specific IB formulation we pursue is analogous to the projection approach of Taira and Colonius [13]: no specific constitutive models are used for the structure so the surface velocity boundary conditions may be freely selected by the user and are enforced without introducing any ad-hoc constants. This approach enables a versatile treatment where various blowing/suction conditions, prescribed surface motions, or compliant structural models may be incorporated with virtually no changes to the overarching formulation.

There are studies that incorporate resolvent and other linearized analysis techniques with IB in a global setting. Hou and Colonius [14] introduced a formulation optimized for spanwise-homogeneous flows, while Shahriar and Shoele

[15] developed an approach for compliant surfaces wherein one layer is assumed spanwise-homogeneous and the others are treated as spanwise-periodic. Goza et al. [16] also performed a global stability analysis with the same projection approach from Taira and Colonius [13] to investigate flag flapping problems. The key source of novelty in our approach is to incorporate this IB treatment into the governing equations for wall-bounded flows, which are homogeneous in the streamwise, spanwise, and temporal directions. This homogeneous property is central to the resolvent analysis of wall-bounded flows, and enables the use of Fourier/Laplace transforms on these variables to yield a set of ordinary differential equations in the wall-normal direction, to significant computational savings.

In this work, we present the IB resolvent formulation for the relatively simple case of flow past a wall with a sinusoidal height variation. This problem is considered to demonstrate the necessary changes needed to utilize a formal IB framework, and we note that a non-IB approach to even this problem would be non-straightforward. We also demonstrate correct implementation of the method for the reference problem of a stationary, flat channel wall for which there are available resolvent results without an IB treatment.

III. Method

A. Mathematical Formulation

The relevant governing equations are the nondimensional incompressible Navier-Stokes and continuity equations,

$$\partial_t \boldsymbol{u}(\boldsymbol{x},t) + (\boldsymbol{u}(\boldsymbol{x},t)\cdot\nabla)\,\boldsymbol{u}(\boldsymbol{x},t) + \nabla p(\boldsymbol{x},t) - \frac{1}{Re}\nabla^2\boldsymbol{u}(\boldsymbol{x},t) = 0, \tag{1}$$

$$\nabla\cdot\boldsymbol{u}(\boldsymbol{x},t) = 0, \tag{2}$$

where $\boldsymbol{x} = [x, y, z]$ represents the set of fluid flow points and the variables $\boldsymbol{u}(\boldsymbol{x},t)$ and $p(\boldsymbol{x},t)$ correspond to the fluid velocity and pressure. Reynolds number is denoted by Re, and the differential operator $\nabla = [\partial_x, \partial_y, \partial_z]$. Typically, boundary conditions are then applied based on the flow configuration. For this work, we set x, y, and z to be the streamwise, wall-normal, and spanwise directions, respectively.

For the IB resolvent method, we use an extended version of these governing equations along with a third no-slip equation (see Taira and Colonius [13]), that enables flow information to be exchanged between the surface and the fluid. Here, $\boldsymbol{\chi} = [\chi_x, \chi_y, \chi_z]$ is the set of spatial coordinates for the surface, Γ, which we take to be a two-dimensional (2D) surface embedded within the 3D flow domain, Ω. Note that as long as the spatially-varying surface Γ has a one-to-one projection onto Γ_0, a flat surface with $\chi_y = 0$, we can parameterize $\boldsymbol{\chi} = [x, g(x), z]$ (see Fig. 1). Here, $g(x)$ is a function that describes the wall-normal-varying geometry of Γ, which we take to be periodic. We note that while the presented formulation is unnecessarily cumbersome for this particular wall configuration, we utilize this more general representation of the surface to enable easier generalization to more complex problem setups (e.g., walls that are time varying and with wall deformations dependent on the spanwise as well as streamwise variable).

Using this characterization of the surface, we may represent the surface stresses and flow velocity along the surface as $\boldsymbol{s}(x,z,t)$ and $\boldsymbol{u}_B(x,z,t)$, respectively. Then the governing equations within the desired IB setting are

$$\partial_t \boldsymbol{u}(\boldsymbol{x},t) + \boldsymbol{u}(\boldsymbol{x},t)\cdot\nabla\boldsymbol{u}(\boldsymbol{x},t) + \nabla p(\boldsymbol{x},t) - \frac{1}{Re}\nabla^2\boldsymbol{u}(\boldsymbol{x},t) = \int_\Gamma \boldsymbol{s}(x',z',t)\delta(\boldsymbol{x} - \boldsymbol{\chi}(x',z',t))\,dx'\,dz', \tag{3}$$

$$\nabla\cdot\boldsymbol{u}(\boldsymbol{x},t) = 0, \tag{4}$$

$$\boldsymbol{u}_B(x',z',t) = \int_\Omega \boldsymbol{u}(\boldsymbol{x},t)\delta(\boldsymbol{x} - \boldsymbol{\chi}(x',z',t))\,d\boldsymbol{x}. \tag{5}$$

To construct the resolvent operator, we assume the flow can be treated as homogeneous in the x, z, and t directions (i.e., it has a steady mean flow that only depends on the wall-normal direction, $\bar{\boldsymbol{u}}(y) = [\bar{u}_x(y), 0, 0]^T$). We represent each flow variable as a mean and fluctuation component; e.g., for the velocity field $\boldsymbol{u}(\boldsymbol{x},t) = \bar{\boldsymbol{u}}(y) + \tilde{\boldsymbol{u}}(\boldsymbol{x},t)$. As in the standard resolvent analysis, only linear quantities in the fluctuating variables are kept in the left-hand-side, and all nonlinear quantities are moved into the right-hand-side and absorbed into a newly defined variable, $\boldsymbol{f}$. The governing equations are then transformed into a single ordinary differential equation in the wall-normal direction following Fourier transforms in the homogeneous (streamwise, spanwise, and time variables) directions. Let $\mathcal{F}_x$ be the Fourier transform in the x direction (analogously defined in z and t) and the vector wavenumber $\boldsymbol{k} = (k_x, k_z, \omega)$ denote the transformed

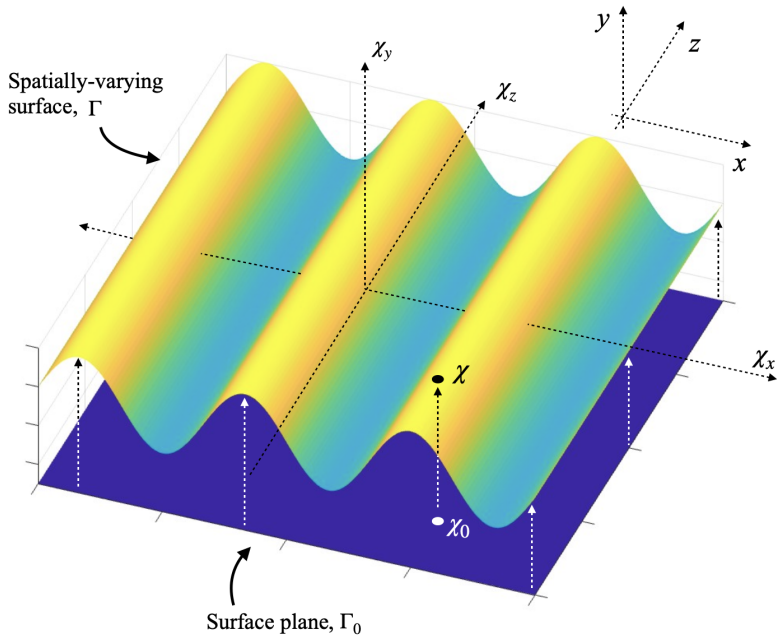

Fig. 1 Schematic of the fluid and surface coordinate systems for a spatially varying surface, Γ, as well as the projected surface plane Γ_0.

streamwise, spanwise, and time variables. Finally, for simplicity denote the x-z-t Fourier transform as $\mathcal{F}_{xzt}(\cdot)$ and define it notationally via a hat as $\hat{(\cdot)}$; e.g., for the velocity variable

$$\hat{\boldsymbol{u}}(y,\boldsymbol{k},t) = \mathcal{F}_{xzt}\left(\boldsymbol{u}(\boldsymbol{x},t)\right) = \int_{-\infty}^{\infty}\int_{-\infty}^{\infty}\int_{-\infty}^{\infty}\boldsymbol{u}(\boldsymbol{x},t)e^{-i(\omega t-k_x x-k_z z)}\,dx\,dz\,dt. \tag{6}$$

When transforming Eqs. (3)–(5), the left-hand-side of Eqs. (3) and (4) leads to the same result as traditional resolvent analysis [7], so we focus on the integral term in Eq. (3) as well as the boundary condition Eq. (5). Starting with Eq. (3), we note that the surface integral can be simplified as

$$\int_{\Gamma}\boldsymbol{s}(x',z',t)\delta(\boldsymbol{x}-\boldsymbol{\chi}(x',z',t))\,dx'\,dz' = \boldsymbol{s}(x,z,t)\delta_g(x,y), \tag{7}$$

where we define $\delta_g(x,y) := \delta(y-g(x))$ for notational simplicity. Applying the Fourier transform to Eq. (7) and applying the convolution theorem, we get

$$\begin{aligned}\int_{-\infty}^{\infty}\int_{-\infty}^{\infty}\int_{-\infty}^{\infty}&\boldsymbol{s}\,(x,z,t)\,\delta_g(x,y)e^{-i(\omega t-k_x x-k_z z)}\,dx\,dz\,dt\\ &= \int_{-\infty}^{\infty}\int_{-\infty}^{\infty}\int_{-\infty}^{\infty}\hat{\boldsymbol{s}}\left(k_x',k_z',\omega'\right)\hat{\delta}_g(y,k_x-k_x',k_z-k_z',\omega-\omega')\,dk_x'dk_z'd\omega', \qquad (8)\\ &= \int_{-\infty}^{\infty}\hat{\boldsymbol{s}}\left(k_x',k_z,\omega\right)\mathcal{F}_x(\delta_g)(y,k_x-k_x')\,dk_x', \qquad (9)\end{aligned}$$

where the last step comes from the fact that $\mathcal{F}_{zt}(\delta_g) = \delta(k_z)\delta(\omega)$. Note the distinction between $\hat{\delta}_g := \mathcal{F}_{xzt}(\delta_g)$ and $\mathcal{F}_x(\delta_g)$.

The no-slip equation, Eq. (5), can be recast as

$$\boldsymbol{u}_B(x',z',t) = \int_{\Omega}\boldsymbol{u}(\boldsymbol{x},t)\delta(\boldsymbol{x}-\boldsymbol{\chi}(x',z',t))\,d\boldsymbol{x} = \int_{-\infty}^{\infty}\boldsymbol{u}\,(\boldsymbol{x},t)\,\delta_g(x,y)\,dy. \tag{10}$$

Applying the Fourier transform in x, z, and t to both sides of the equation yields, by a similar set of steps as in Eqs. (8) and (9),

$$\hat{\boldsymbol{u}}_B(k_x, k_z, \omega) = \int_{-\infty}^{\infty} \int_{-\infty}^{\infty} \hat{\boldsymbol{u}}(y, k'_x, k_z, \omega) \mathcal{F}_x(\delta_g)(y, k_x - k'_x)\, dk'_x\, dy. \tag{11}$$

Note the transformed no-slip equation Eq. (11) contains both an integral over k'_x and y, meaning that the final resolvent operator will have to account for both variables. This point is in contrast to the source term Eq. (9), which is formally singular. This distinction is analogous to the result that arises for the IB framework in high-fidelity simulations.

The Fourier transformed boundary condition Eq. (11), in conjunction with the transformed variants of the governing momentum and mass equations Eqs. (3) and (4) (accounting for the transform of the surface stress term Eq. (9)), constitute a set of ordinary differential equations in the y direction to be solved. The various operators in this system of ordinary differential equations may be discretized in the standard ways. In this work, we utilize a stretched grid of discrete points along the y-direction described further in Sec. IV. This discretization yields a set of unknowns which remain continuous functions of the wavenumber $\boldsymbol{k}$ but are evaluated at the discrete points, e.g. $\hat{\mathbf{u}}_x = [u_{x,1}, ..., u_{x,n_y}]^T$, with analogous definitions for $\hat{\mathbf{u}}_y$, $\hat{\mathbf{u}}_z$, and $\hat{\mathbf{p}}$ as well as each of the forcing directions, surface stresses, and wall velocity terms.

Through this discretization process, derivative and integral operators are approximated as matrices. The matrices for the non-IB operators are well known [7]; the details of their form are left out but the results are summarized in the Appendix. For the IB operators associated Eqs. (9) and (11), we must account for the fact that in general the flow grid will not align with the surface points by replacing the true Dirac delta function with a regularized delta function that has nonzero support over a small number of flow grid points (we detail our choice of regularized delta function in Sec. IV below). Additionally, the integrals must be approximated, which can be done using standard quadrature techniques. The result of this discretization process is a set of linear equations

$$\begin{aligned}
&\begin{bmatrix}
\mathbf{L}(k_{x,1}, k_z, \omega) & \mathbf{R}(k_{x,1}, k_{x,1}) & \dots & \mathbf{0} & \mathbf{R}(k_{x,1}, k_{x,n_{k_x}}) \\
\mathbf{E}(k_{x,1}, k_{x,1}) & \mathbf{0} & \dots & \mathbf{E}(k_{x,1}, k_{x,n_{k_x}}) & \mathbf{0} \\
\vdots & \vdots & \ddots & \vdots & \vdots \\
\mathbf{0} & \mathbf{R}(k_{x,n_{k_x}}, k_{x,1}) & \dots & \mathbf{L}(k_{x,n_{k_x}}, k_z, \omega) & \mathbf{R}(k_{x,n_{k_x}}, k_{x,n_{k_x}}) \\
\mathbf{E}(k_{x,n_{k_x}}, k_{x,1}) & \mathbf{0} & \dots & \mathbf{E}(k_{x,n_{k_x}}, k_{x,n_{k_x}}) & \mathbf{0}
\end{bmatrix}
\begin{bmatrix}
\hat{\mathbf{q}}(k_{x,1}, k_z, \omega) \\
\hat{\mathbf{s}}(k_{x,1}, k_z, \omega) \\
\vdots \\
\hat{\mathbf{q}}(k_{x,n_{k_x}}, k_z, \omega) \\
\hat{\mathbf{s}}(k_{x,n_{k_x}}, k_z, \omega)
\end{bmatrix} \\
&\qquad = \begin{bmatrix}
\mathbf{B}_f & \mathbf{0} & \dots & \mathbf{0} & \mathbf{0} \\
\mathbf{0} & \mathbf{B}_{\mathrm{IB}} & \dots & \mathbf{0} & \mathbf{0} \\
\vdots & \vdots & \ddots & \vdots & \vdots \\
\mathbf{0} & \mathbf{0} & \dots & \mathbf{B}_f & \mathbf{0} \\
\mathbf{0} & \mathbf{0} & \dots & \mathbf{0} & \mathbf{B}_{\mathrm{IB}}
\end{bmatrix}
\begin{bmatrix}
\hat{\mathbf{f}}(k_{x,1}, k_z, \omega) \\
\hat{\mathbf{u}}_B(k_{x,1}, k_z, \omega) \\
\vdots \\
\hat{\mathbf{f}}(k_{x,n_{k_x}}, k_z, \omega) \\
\hat{\mathbf{u}}_B(k_{x,n_{k_x}}, k_z, \omega)
\end{bmatrix},
\end{aligned} \tag{12}$$

where $\hat{\mathbf{q}}$ represents the state vector given by the concatenation of the velocity and pressure variables, and the forcing terms (exogenous forcing on momentum and mass conservation equations, and nonlinear forcing due to advection in the conservation of momentum) have been grouped into $\hat{\mathbf{f}}$. The $\mathbf{L}$ operator represents the usual non-IB resolvent matrices [7], whereas the $\mathbf{R}$ and $\mathbf{E}$ matrices represent the quadrature operations associated with the $\mathcal{F}_x(\delta_g)$ kernel in Eqs. (3) and (5). These matrices are described in further detail in the Appendix, along with $\mathbf{L}$. We also include a matrix on the right-hand-side (that involves the $\mathbf{B}_f$, $\mathbf{B}_{\mathrm{IB}}$ terms that premultiply the nonlinear unknowns). This matrix is written generally to enable various forcing on the linear terms; its specific form for the channel flow problem of interest will be discussed in the next section.

There are two important distinctions from a standard resolvent analysis in the matrix system Eq. (12). The first difference is the appearance of the IB operators $\mathbf{R}$ and $\mathbf{E}$ that arise to respectively convey the surface stresses from the wall onto the fluid, and to explicitly incorporate the no-slip condition into the governing equations such that when the flow velocity is interpolated onto the wall surface the result equals the wall velocity. The second major difference is that the equations are coupled across all k_x wavenumbers, a feature that arises because of the convolution in the Fourier-transformed no-slip condition Eq. (11). Note that if the wall displacement were a function of the spanwise direction or time, there would be coupling across those wavenumber variables as well. By contrast, it is instructive to consider how the equations simplify in the conventional case of a stationary, flat wall. In this configuration $\chi_y \equiv 0$ for every $(\chi_x, \chi_z) = (x, z)$, *i.e.* $\delta(y - g(x)) = \delta(y)$ is no longer dependent on x and the convolution in the expressions Eqs.

(9) and (11) collapses to a single value. As such, the governing resolvent equations simplify to have no wavenumber coupling as

$$\begin{bmatrix} \mathbf{L}(k_x, k_z, \omega) & \mathbf{R}_{\text{flat}} \\ \mathbf{E}_{\text{flat}} & \mathbf{0} \end{bmatrix} \begin{bmatrix} \hat{\mathbf{q}}(k_x, k_z, \omega) \\ \hat{\mathbf{s}}(k_x, k_z, \omega) \end{bmatrix} = \begin{bmatrix} \mathbf{B}_f & \mathbf{0} \\ \mathbf{0} & \mathbf{B}_{\text{IB}} \end{bmatrix} \begin{bmatrix} \hat{\mathbf{f}}(k_x, k_z, \omega) \\ \hat{\mathbf{u}}_B(k_x, k_z, \omega) \end{bmatrix}, \tag{13}$$

where $\mathbf{R}_{\text{flat}}$ and $\mathbf{E}_{\text{flat}}$ are identical to $\mathbf{R}$ and $\mathbf{E}$ except the $\mathcal{F}_x(\delta_g)$ terms have been replaced by $\delta(y)$. While the IB formulation requires these operators to remain, the cross-wavenumber coupling disappears.

IV. Results: flat channel wall

The IB resolvent formulation was coded in MATLAB; it constructs the resolvent system in Eq. (12) and takes the singular value decomposition of the matrix system using built-in MATLAB functions. This results in a set of response modes Ψ and forcing modes Φ. For the y-grid we use a set of fine, uniformly spaced points around the lower IB wall ($y = [-1.015, -0.9897]$) with $\Delta y = 1.693 \times 10^{-4}$ to ensure accuracy when handling the delta function. This spacing is mirrored onto the upper wall for the sake of symmetry and the interior points between wall sections are defined by a hyperbolic tangent stretching function with a stretching factor of 2.6. Our choice of regularized delta function is originally described in Roma et al. [17], and is given by

$$\delta_h(y) = \begin{cases} \frac{1}{6\Delta y}\left(5 - 3\frac{|y|}{\Delta y} - \sqrt{-3\left(1 - \frac{|y|}{\Delta y}\right)^2 + 1}\right), & \frac{1}{2}\Delta y \le |y| \le \frac{3}{2}\Delta y, \\ \frac{1}{3\Delta y}\left(1 + \sqrt{-3\left(\frac{y}{\Delta y}\right)^2 + 1}\right), & |y| \le \frac{1}{2}\Delta y, \\ 0, & \text{otherwise.} \end{cases} \tag{14}$$

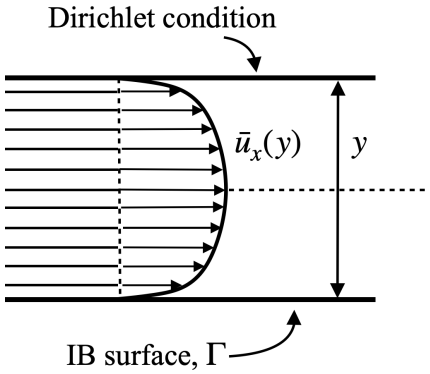

Fig. 2 Schematic of the flat-wall channel problem. The upper surface ($y = 1$) uses a traditional Dirichlet condition while the lower surface $y = -1$ uses the IB framework.

As a test of the underlying IB treatment, for the first example problem we consider a flat-walled channel ranging from $y \in [-1, 1]$, where the length scale is normalized by the half-channel height h. Solid no-slip walls are located at $y = -1$ and $y = 1$. Note the y domain is simulated over a slightly larger range $y \in [-1.015, 1.015]$ than the channel both to provide sufficient support for the delta function and accommodate the wall deformations in later examples. While the additional range is not necessary at the upper wall, we include it to preserve symmetry in domain size. The mean flow is calculated from the same eddy-viscosity profile used by Moarref et al. [18],

$$\bar{u}_x(y) = Re_\tau \int_0^{y+1} \frac{1-\xi}{1+\nu_T(\xi)}\, d\xi, \quad y \in [-1, 1] \tag{15}$$

$$\nu_T(y) = \frac{1}{2}\left(1 + \left(\frac{\kappa Re_\tau}{3}\left(2y - y^2\right)\left(3 - 4y + 2y^2\right)\left(1 - e^{(|y-1|-1)Re_\tau/\alpha}\right)\right)^2\right)^{1/2} - \frac{1}{2}, \tag{16}$$

where κ is the von Kármán constant. Note that the generated mean flow is already normalized by the friction velocity u_τ and that it is set to zero outside $y = [-1, 1]$ since it is meant for the simulation of perfectly flat walls. We also assume the mean is constant in x given the small size of the wall deformations.

We consider a friction Reynolds number of $Re_\tau = u_\tau h/\nu = 186$, where ν is the kinematic viscosity, wavenumbers $k_x = 1$, $k_z = 11.69$, and frequency $\omega = 10$. Parameters have been selected to correspond to the most energetic energy scales for the buffer layer of wall-bounded turbulence, $\lambda_x^+ \approx 1170$ and $\lambda_z^+ \approx 100$ with wavespeed $\omega^+/k_x^+ \approx 19$, where the superscript + indicates normalization by u_τ and ν.

Note that in traditional resolvent analysis, the Dirichlet boundary conditions at the channel walls are enforced by replacing the linearized equations for rows corresponding to $y = \pm 1$ with a linear equation for the boundary condition. For the example problem, we set the IB surface with $\hat{\boldsymbol{u}}_B = 0$ at the lower wall ($y = -1$) and use the traditional Dirichlet boundary condition for the upper wall ($y = 1$) (see Fig. 2). This results in mass matrix entries

$$\mathbf{B}_f = \begin{bmatrix} \mathbf{I} & \mathbf{0} & \mathbf{0} & \mathbf{0} \\ \mathbf{0} & \mathbf{I} & \mathbf{0} & \mathbf{0} \\ \mathbf{0} & \mathbf{0} & \mathbf{I} & \mathbf{0} \\ \mathbf{0} & \mathbf{0} & \mathbf{0} & \mathbf{0} \end{bmatrix}, \quad \mathbf{B}_{\mathrm{IB}} = \mathbf{0}. \tag{17}$$

Figure 3 shows the singular values for the flat channel wall from the IB resolvent are nearly identical to those calculated with traditional resolvent analysis. Similarly, Figs. 4a and 4b show good agreement for the first response and forcing mode respectively. In both cases, we can observe symmetric behavior within the flow: the singular values occur in pairs, and although the modes at the upper wall are not pictured, they exhibit modes identical (mirrored) to those at the lower wall. The symmetry in both the grid and geometry for the traditional resolvent analysis is reflected in the fact that the first two modes are an orthogonal linear combination of the modes isolated to either wall. Special treatment is needed to separate the mode pairs into isolated pairs. However, in the IB resolvent case, the loss in symmetry in the boundary conditions (due to the IB handling of the lower wall) causes the pair of modes to separate naturally. This is also true for the example of the sinusoidal lower wall (Sec. V), which breaks the symmetry in geometry and results in different singular values for modes isolated to either wall.

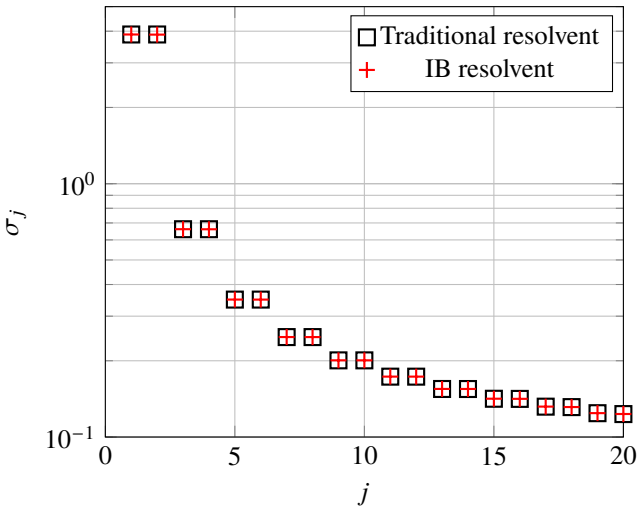

Fig. 3 Singular values obtained for turbulent flat channel flow at $Re_\tau = 186$ and $k_x = 1$ from the IB resolvent (red crosses) and traditional resolvent analysis (black squares).

V. Results: sinusoidal channel wall

Now consider the case of a sinusoidal lower wall (Fig. 5) described by the function $g(x) = -1 + A_0 \sin(2\pi k_g x)$, with varying wall amplitude A_0 and wavenumber $k_g = 1$. While the sinusoidal wall requires a convolution over multiple spatial wavenumbers, we first focus on the use of a single wavenumber, $k_x = 1$, to characterize the influence of wall

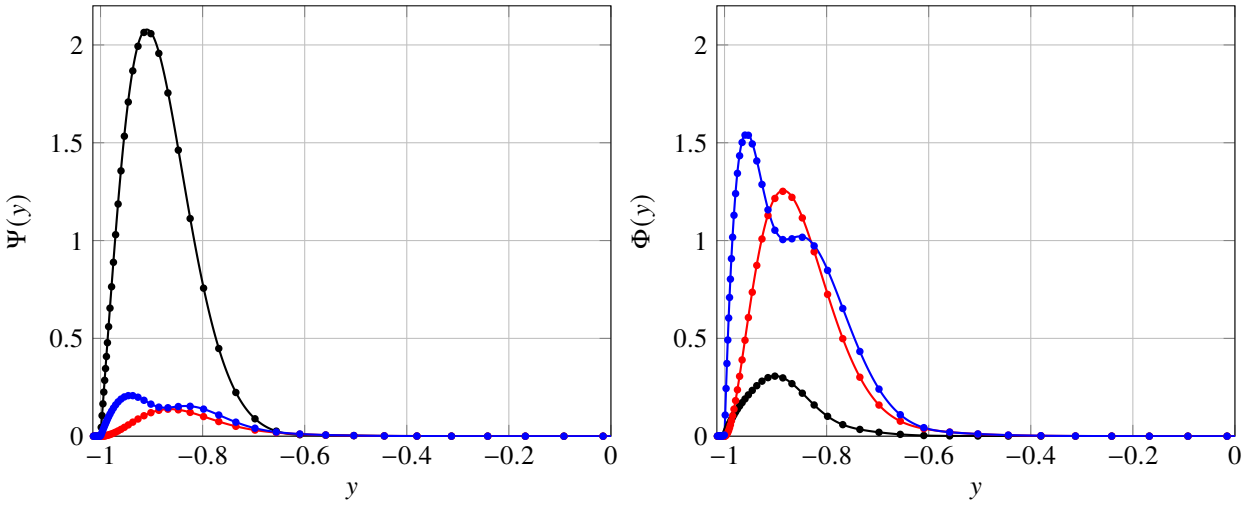

(a) (b)

Fig. 4 (a) Principal response mode corresponding to u_x (black), u_y (red), and u_z (blue) calculated via traditional resolvent analysis (lines) and IB resolvent (markers) for the flat channel wall at $k_x = 1$. (b) Principal forcing mode corresponding to f_x (black), f_y (red), and f_z (blue) calculated via traditional resolvent analysis (lines) and IB resolvent (markers) for the flat channel wall at $k_x = 1$.

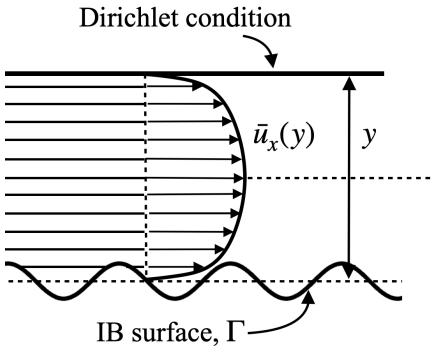

Fig. 5 Schematic of the sinusoidal wall channel problem. The upper surface ($y = 1$) uses a traditional Dirichlet condition while the lower sinusoidal surface $y = -1$ uses the IB framework.

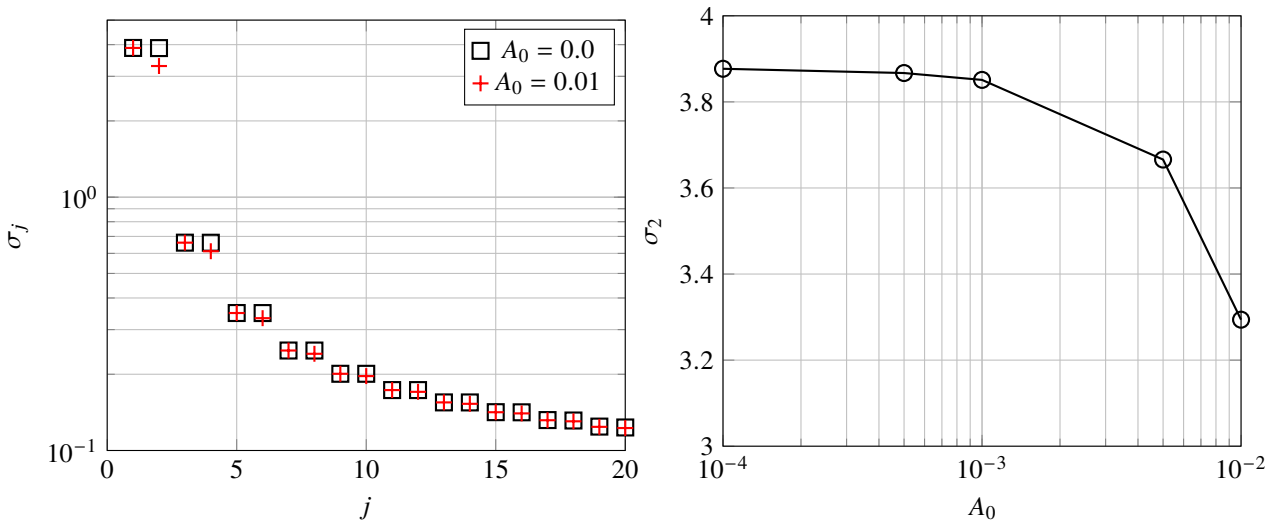

(a) **(b)**

Fig. 6 (a) Singular values for the sinusoidal channel wall at $k_x = 1$ with varying wall amplitudes $A_0 = 0.01$ (red crosses) and $A_0 = 0$ (black squares). (b) Second singular value for the sinusoidal channel wall as a function of A_0.

amplitude on the most energetically relevant wavenumber in the flat wall case. Figure 6a shows that for $A_0 = 0.01$ the singular values associated with the lower wall (second in each pair) decrease compared to the corresponding values for the flat wall. This decrease is most significant for the leading singular value associated with the sinusoidal wall, σ_2, with the value at higher modes exhibiting increasingly less change compared to the flat wall case. Figure 6b depicts the value of σ_2 as a direct function of wall amplitude A_0, demonstrating a logarithmic relationship between the two values. This de-pairing of singular values is a direct consequence of the break in geometric symmetry at the top and bottom walls, and the implications of this outcome on the modal shapes will be discussed next.

Figure 7a provides the u_x response mode for three different wall amplitudes $A_0 = [0.0, 0.001, 0.01]$. There is no significant change at the upper flat wall, as expected, but there is a slight shift in the peak at the lower wall towards the channel center for large A_0. An additional peak also forms in the region of the sinusoidal wall, reflective of flow structures arising in response to the corrugated surface. Note that the isolated region of nonzero flow near the bottom wall begins within the nominal amplitude of the sinusoidal wall and extends to the bottom surface at $y = -1.015$. This extension of nonzero flow is an outcome of utilizing the mean flow from the undeformed configuration. This mean flow is nonzero down to the undeflected wall location, which extends below the wall in the sinusoidal location and drives small-amplitude flow in the small region below the wall. This choice of the mean state from the flat-wall configuration is appropriate when the deformed configuration primarily affects the fluctuating quantities rather than the mean. A similar ansatz of adopting the flat-wall mean state was used for compliant walls in Luhar et al. [9].

The u_y response mode (Figure 7b) shows a similar set of features (increased response around $y = -1$ and a slight shift towards the channel center), but the peak for the lower wall also appears to increase in magnitude. This increased peak, also observable in other response and forcing modes (not pictured), suggests a greater flow receptivity to wall perturbations in the wall-normal direction.

With this understanding for the case of a single spatial wavenumber, we now assess the importance of including the additional wavenumbers involved in the convolution in Eqs. (9) and (11). In principle, all wavenumber combinations with the target wavenumber must be considered, though we assess the convergence of the result by keeping a few additional harmonics $k_x = [1, 2, 3]$. We first investigate the results for the flat channel using IB resolvent (coupling all three wavenumbers), compared to those of the traditional resolvent calculated for each k_x wavenumber separately and then concatenated. Figure 8a demonstrates that the singular values across these two cases match well. This outcome reflects the physical result that at $A_0 = 0$ the various wavenumbers physically decouple and the traditional resolvent result is recovered.

Figure 8b now probes the effect of considering multiple wavenumbers for a nonzero wall amplitude of $A_0 = 0.01$.

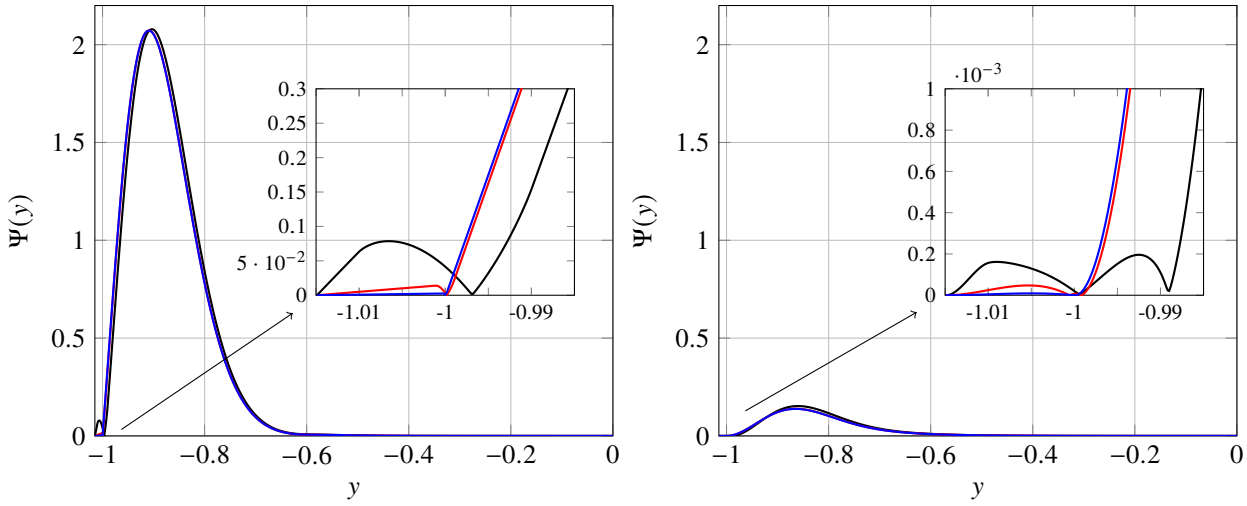

Fig. 7 (a) Principal response mode corresponding to u_x for wall amplitudes $A_0 = 0.01$ (black), $A_0 = 0.001$ (red), and $A_0 = 0.0$ (blue) for the sinusoidal channel wall at $k_x = 1$. Inset shows a zoomed view of the outer plot for $y \in [-1.015, -0.985]$. (b) Principal response mode corresponding to u_y for wall amplitudes $A_0 = 0.01$ (black), $A_0 = 0.001$ (red), and $A_0 = 0.0$ (blue) for the sinusoidal channel wall at $k_x = 1$. Inset shows a zoomed view of the outer plot for $y \in [-1.015, -0.985]$.

Even for this case where there is nominally cross-wavenumber coupling, the singular values obtained by considering a single wavenumber accurately approximate the result that accounts for all of their coupling. This outcome demonstrates that the effect of the sinusoidal wall can be reasonably approximated by calculations involving each individual wavenumber of interest, without the effect of coupling from other wavenumbers. Moreover, the singular values are still dominated by the first harmonic wavenumber $k_x = 1$. Finally, Fig. 9 shows that the u_x response mode utilizing all three wavenumbers closely matches the response mode for $k_x = 1$, with small exceptions very near the sinusoidal wall.

VI. Conclusion

We formally integrated an immersed boundary (IB) formalism into resolvent analysis for sinusoidal surfaces, in a manner that can be extended to more complex surface geometries and motions, potentially with dynamics coupled to the flow. This approach is a first step towards a framework that can treat a variety of heterogeneous surface designs, compliant materials, and surface actuation strategies with minimal modifications to the formulation. The framework contains the main components of the traditional resolvent operator, along with new matrices that account for the influence of the surface boundary condition and induced fluid forces on one another. We emphasize that these new IB terms are sparse and facilitate a tractable solution process.

The proposed IB resolvent framework was tested on the flat-walled channel problem described in Moarref et al. [18], and the results were compared with traditional (non-IB) resolvent. Both the singular values and modes matched closely across the two methods. The method was then applied to a modified version of the flat-walled channel with a sinusoidal surface in place of the lower flat wall. The IB resolvent produced modes similar to the flat wall case, but with an additional peak in both the response and forcing modes centered around the sinusoidal wall, with magnitude increasing for larger wall amplitudes as expected. Finally it was demonstrated that for the convolution over multiple wavenumbers that appears in this formulation, each mode of the IB resolvent was almost completely captured by accounting only for the effect of a single wavenumber, the first harmonic of the surface wavenumber (and no cross-frequency terms). This outcome suggests that the proposed approach can be computed by considering very few or no additional wavenumber terms, resulting in a small change in cost to the traditional resolvent formulation.

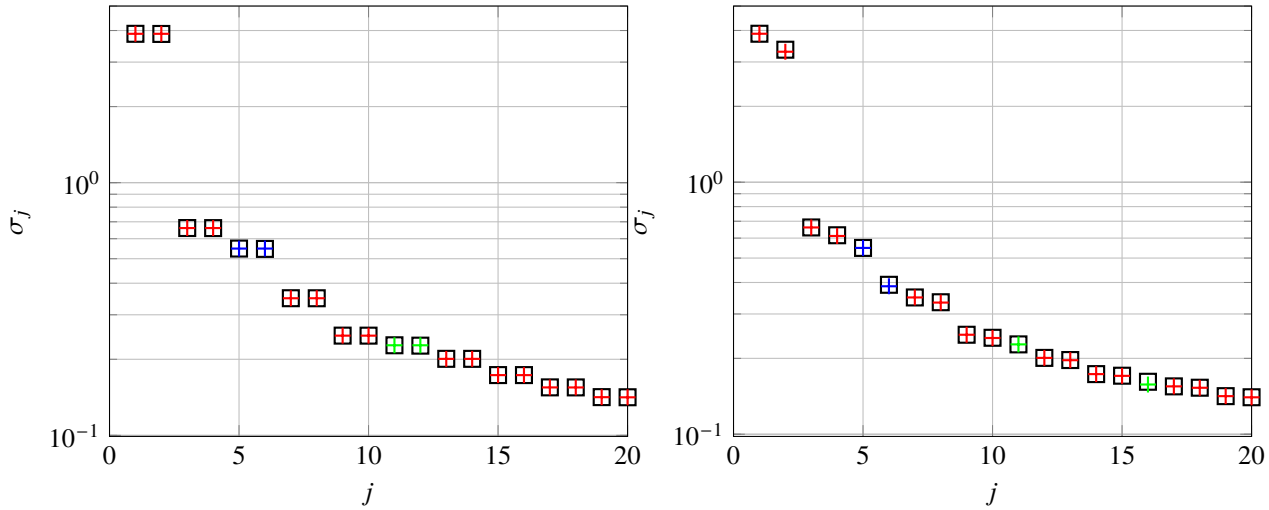

Fig. 8 (a) Singular values for flat wall channel obtained with IB resolvent (black squares) at joint wavenumbers $k_x = [1, 2, 3]$ and traditional resolvent analysis (crosses) at individual wavenumbers $k_x = 1$ (red) and $k_x = 2$ (blue) and $k_x = 3$ (green). (b) Singular values for sinusoidal wall channel ($A_0 = 0.01$) obtained with IB resolvent at joint wavenumbers (black squares) $k_x = [1, 2, 3]$ and individual wavenumbers (crosses) $k_x = 1$ (red), $k_x = 2$ (blue) and $k_x = 3$ (green).

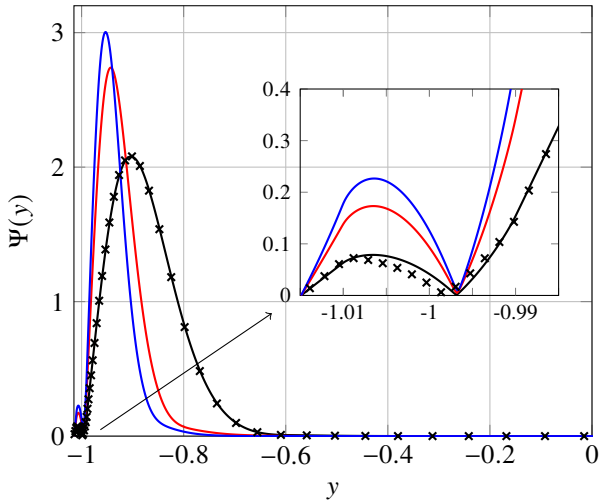

Fig. 9 Principal response modes corresponding to u_x for the sinusoidal wall channel with amplitude $A = 0.01$ at combined wavenumbers $k_x = [1, 2, 3]$ (black crosses) and individual wavenumbers (solid) $k_x = 1$ (black), $k_x = 2$ (red), and $k_x = 3$ (blue).

Acknowledgments

The authors gratefully acknowledge funding from AFOSR under the MURI program, grant number AF FA9550-23-1-0299.

Appendix

A. Delta function Fourier transform

If we assume the wall can be written as a periodic function $g(x)$ with wavenumber k_g, (generally distinct from k_x), the delta function applied to this periodic function is equivalent to a delta comb, or a sum of delta functions at the zeros of $(y - g(x))$. For any periodic function $g(x)$, the zeros of $(y - g(x))$ can be defined as $x_{0,n}$, $n \in \mathbb{Z}$ (the set of integers). Therefore, the delta comb is

$$\delta_g(x, y) = \sum_{n=-\infty}^{\infty} \delta(x - x_{0,n}). \tag{18}$$

The Fourier transform of the delta comb is another delta comb, defined by

$$\mathcal{F}_x(\delta_g)(y, k_x' - k_x) = \frac{1}{\sqrt{2\pi}} \sum_{m=-\infty}^{\infty} \left(e^{i(k_x' - k_x)x_{0,m}} \right). \tag{19}$$

Note that the convolution of the delta term with surface stress in Eq. (9) and velocity in Eq. (11) will result in the delta comb as a function of $k_x' - k_x$ rather than k_x on its own as it would be otherwise.

B. Submatrix defintions

The $\mathbf{L}$ block matrix is identical to the one presented in McKeon and Sharma (2010) with the first three rows corresponding to the x, y, z components for Navier Stokes, and the fourth row representing continuity,

$$\mathbf{L} = \begin{bmatrix} -i\omega\mathbf{I} + \mathbf{L}_0 & \mathbf{D}_{(1)}\bar{\boldsymbol{u}} & 0 & ik_x\mathbf{I} \\ 0 & -i\omega\mathbf{I} + \mathbf{L}_0 & 0 & \mathbf{D}_{(1)} \\ 0 & 0 & -i\omega\mathbf{I} + \mathbf{L}_0 & ik_z\mathbf{I} \\ ik_x\mathbf{I} & \mathbf{D}_{(1)} & ik_z\mathbf{I} & 0 \end{bmatrix}, \quad \mathbf{L}_0 = ik_x\bar{\boldsymbol{u}}\mathbf{I} + \frac{1}{Re}\left(\kappa^2\mathbf{I} - \mathbf{D}_{(2)}\right). \tag{20}$$

The $\mathbf{D}_{(1)}$ and $\mathbf{D}_{(2)}$ matrices corresponding to the first and second derivatives are constructed with finite difference methods. Note since we are using a non-uniform grid, the matrices are defined as

$$\mathbf{D}_{(1)}(i,j) = \begin{cases} \frac{-3}{|y_3 - y_1|}, & i = 1, j = 1, \\ \frac{4}{|y_3 - y_1|}, & i = 1, j = 2, \\ \frac{-1}{|y_3 - y_1|}, & i = 1, j = 3, \\ \frac{1}{|y_{n_y} - y_{n_y-2}|}, & i = n_y, j = n_y - 2, \\ \frac{-4}{|y_{n_y} - y_{n_y-2}|}, & i = n_y, j = n_y - 1, \\ \frac{3}{|y_{n_y} - y_{n_y-2}|}, & i = n_y, j = n_y, \\ \frac{-1}{|y_{n_{i+1}} - y_{n_{i-1}}|}, & i = [2, n_y - 1], j = i - 1, \\ \frac{1}{|y_{n_{i+1}} - y_{n_{i-1}}|}, & i = [2, n_y - 1], j = i + 1, \\ 0, & \text{otherwise}, \end{cases}, \tag{21}$$

$$\mathbf{D}_{(2)}(i,j) = \begin{cases} \frac{-1}{|y_2-y_1|^2}, & i=1, j=1, \\ \frac{4}{|y_2-y_1|^2}, & i=1, j=2, \\ \frac{-5}{|y_2-y_1|^2}, & i=1, j=3, \\ \frac{2}{|y_2-y_1|^2}, & i=1, j=4, \\ \frac{-2}{|y_{n_y}-y_{n_y-1}|^2}, & i=n_y, j=n_y-3, \\ \frac{5}{|y_{n_y}-y_{n_y-1}|^2}, & i=n_y, j=n_y-2, \\ \frac{-4}{|y_{n_y}-y_{n_y-1}|^2}, & i=n_y, j=n_y-1, \\ \frac{1}{|y_{n_y}-y_{n_y-1}|^2}, & i=n_y, j=n_y, \\ \frac{-2}{|y_{i+1}-y_{i-1}|}\left(\frac{1}{|y_i-y_{i-1}|}+\frac{1}{|y_{i+1}-y_i|}\right), & i=[2,n_y-1], j=i, \\ \frac{2}{|y_i-y_{i-1}||y_{i+1}-y_{i-1}|}, & i=[2,n_y-1], j=i-1, \\ \frac{2}{|y_{i+1}-y_i||y_{i+1}-y_{i-1}|}, & i=[2,n_y-1], j=i+1, \\ 0, & \text{otherwise.} \end{cases} \tag{22}$$

Each entry of $\mathbf{L}$ is a $n_y \times n_y$ matrix containing variables changing along y. The matrices

$$\mathbf{R}(k_x,k_x') = \begin{bmatrix} \mathbf{R}_0(k_x,k_x') & 0 & 0 \\ 0 & \mathbf{R}_0(k_x,k_x') & 0 \\ 0 & 0 & \mathbf{R}_0(k_x,k_x') \\ 0 & 0 & 0 \end{bmatrix}, \quad \mathbf{E}(k_x,k_x') = \begin{bmatrix} \mathbf{E}_0(k_x,k_x') & 0 & 0 & 0 \\ 0 & \mathbf{E}_0(k_x,k_x') & 0 & 0 \\ 0 & 0 & \mathbf{E}_0(k_x,k_x') & 0 \end{bmatrix}, \tag{23}$$

where

$$\mathbf{R}_0(k_x,k_x') = \Delta k_x \begin{bmatrix} \mathcal{F}_x(\delta_g^h)(y_1, k_x-k_x') \\ \vdots \\ \mathcal{F}_x(\delta_g^h)(y_{n_y}, k_x-k_x') \end{bmatrix}, \quad \mathbf{E}_0(k_x,k_x') = \Delta k_x \begin{bmatrix} \mathcal{F}_x(\delta_g^h)(y_1, k_x-k_x')\Delta y_1 \\ \vdots \\ \mathcal{F}_x(\delta_g^h)(y_{n_y}, k_x-k_x')\Delta y_{n_y} \end{bmatrix}^T, \tag{24}$$

contain the delta comb components for the Navier Stokes and no-slip equations. These matrices are zero everywhere except the diagonal, allowing for a sparse resolvent operator. Note that while the formulation is derived in the continuous setting, the discrete numerical implementation requires regularized delta functions, denoted δ^h.

References

[1] Lin, J. C., "Review of research on low-profile vortex generators to control boundary-layer separation," *Progress in Aerospace Sciences*, Vol. 38, No. 4-5, 2002, pp. 389–420.

[2] Viswanath, P. R., "Aircraft viscous drag reduction using riblets," *Progress in Aerospace Sciences*, Vol. 38, No. 6-7, 2002, pp. 571–600.

[3] Gursul, I., Wang, Z., and Vardaki, E., "Review of flow control mechanisms of leading-edge vortices," *Progress in Aerospace Sciences*, Vol. 43, No. 7–8, 2007, pp. 246–270.

[4] Koklu, M., and Owens, L. R., "Comparison of Sweeping Jet Actuators with DifferentFlow-Control Techniques for Flow-Separation Control," *AIAA Journal*, Vol. 55, No. 3, 2017.

[5] Hussein, M. I., Biringen, S., Bilal, O. R., and Kucala, A., "Flow stabilization by subsurface phonons," *Proceedings of the Royal Society A*, Vol. 471, 2015.

[6] Park, S., Hristov, G., Balasubramanian, S., Goza, A., Ansell, P. J., and Matlack, K., "Design and Analysis of Phononic Material for Passive Flow Control," *AIAA AVIATION 2022 Forum*, AIAA, Chicago, IL, 2022, p. 3330. https://doi.org/10.2514/6.2022-3330, URL https://arc.aiaa.org/doi/abs/10.2514/6.2022-3330.

[7] McKeon, B. J., and Sharma, A. S., "A critical-layer framework for turbulent pipe flow," *Journal of Fluid Mechanics*, Vol. 658, 2010, pp. 336–382.

[8] Chavarin, A., and Luhar, M., "Resolvent Analysis for Turbulent Channel Flow with Riblets," *AIAA Journal*, Vol. 58, No. 2, 2020.

[9] Luhar, M., Sharma, A. S., and McKeon, B. J., "A framework for studying the effect of compliant surfaces on wall turbulence," *Journal of Fluid Mechanics*, Vol. 768, 2015, pp. 415,441.

[10] Jafari, A., McKeon, B. J., and Arjomandi, M., "Frequency-tuned surfaces for passive control of wall-bounded turbulent flow – a resolvent analysis study," *Journal of Fluid Mechanics*, Vol. 959, 2023, p. A26.

[11] Luhar, M., Sharma, A. S., and McKeon, B. J., "Opposition control within the resolvent analysis framework," *Journal of Fluid Mechanics*, Vol. 749, 2014, pp. 597–626.

[12] Peskin, C. S., "Flow patterns around heart valves: A numerical method," *Journal of Computational Physics*, Vol. 10, No. 2, 1972, pp. 252–271.

[13] Taira, K., and Colonius, T., "The immersed boundary method: A projection approach," *Journal of Computational Physics*, Vol. 225, No. 2, 2007, pp. 2118 – 2137.

[14] Hou, W., and Colonius, T., "Three-dimensional Stability and Resolvent Analyses of External Flows Over Spanwise-homogeneous Immersed Bodies," *AIAA AVIATION 2023 Forum*, AIAA, San Diego, CA, 2023, p. 3414. https://doi.org/10.2514/6.2023-3414, URL https://arc.aiaa.org/doi/abs/10.2514/6.2023-3414.

[15] Shahriar, A., and Shoele, K., "A framework for studying turbulent boundary layer interaction with anisotropic compliant surface," *Proceedings of the Summer Program 2022*, 2022.

[16] Goza, A., Colonius, T., and Sader, J. E., "Global modes and nonlinear analysis of inverted-flag flapping," *Journal of Fluid Mechanics*, Vol. 857, 2018, pp. 312–344.

[17] Roma, A. M., Peskin, C. S., and Berger, M. J., "An Adaptive Version of the Immersed Boundary Method," *Journal of Computational Physics*, Vol. 153, 1999, pp. 509–534.

[18] Moarref, R., Sharma, A. S., Tropp, J. A., and McKeon, B. J., "Model-based scaling of the streamwise energy density in high-Reynolds-number turbulent channels," *Journal of Fluid Mechanics*, Vol. 734, 2013, pp. 275–316.